

X-ray Emission from the Interstellar and Circumgalactic Medium of Elliptical Galaxies based on *MACER* simulations

Aditi Vijayan^{1,2}, [★], Bocheng Zhu^{1,3}, Miao Li⁴, [†], Feng Yuan^{1,3}, [‡], and Luis C. Ho^{5,6}

¹*Shanghai Astronomical Observatory, Chinese Academy of Sciences, Shanghai 200030, People's Republic of China*

²*Research School of Astronomy and Astrophysics, Australian National University, Canberra ACT 2601, Australia*

³*University of Chinese Academy of Sciences, 19A Yuquan Road, Beijing 100049, People's Republic of China*

⁴*Zhejiang University*

⁵*Kavli Institute for Astronomy and Astrophysics, Peking University, Beijing 100871, People's Republic of China*

⁶*Department of Astronomy, School of Physics, Peking University, Beijing 100871, People's Republic of China*

Accepted XXX. Received YYY; in original form ZZZ

ABSTRACT

Interstellar (ISM) and circumgalactic medium (CGM) around galaxies are linked to several physical processes that drive galaxy evolution. For example, the X-ray emission from the CGM gas around ellipticals has been linked to the AGN feedback occurring in the host. Upcoming telescopes such as HUBS, with ~ 1 eV resolution, can provide us with deep insights about the hot gas properties of such galaxies thus constrain these processes. In this project, we discuss X-ray emission of the ISM and CGM of elliptical galaxies simulated using *MACER* code. We generate X-ray emission data from the *MACER* simulations with various feedback models and produce mock observations for an instrument with high spectral resolution, which is a necessary step of selecting sources for the future observations with planned mission such as HUBS. More importantly, we establish connections between the physics of AGN and stellar feedback with the emission spectra from the ISM and CGM to investigate the possibility of using observations to constrain feedback models. We fit the X-ray spectra from these simulations with standard fitting procedures and compare the retrieved physical properties with their counterparts from the simulations to understand whether the future high-resolution observations can reliably reveal the properties of the gas in the galaxies.

Key words: Active galactic nuclei(16), Circumgalactic medium(1879), X-ray observatories(1819), Elliptical galaxies(456), Hydrodynamical simulations(767)

1 INTRODUCTION

Feedback processes occurring in a galaxy as a result of the activity of the central Active Galactic Nucleus (AGN) are known to affect the evolution of the host galaxy. These processes are driven by the interaction of the radiation, wind and jet outputs from the AGN with the gas in the galaxy. Energetically, a large fraction ($\sim 10\%$) of the mass accreted onto the supermassive black hole (SMBH) is converted into energy for powering the AGN. Because this energy is significantly larger than the binding energy of gas in the galaxy, an AGN strongly impacts the gas distribution host galaxy (Fabian 2012).

Several observations indicate the effect an AGN has on its host. For relatively larger objects, such as clusters and groups, scalings between the black hole mass (M_\bullet) and the halo temperatures are explained only by invoking AGN feedback as a source of additional heating to the gas (Bogdán et al. 2018; Gaspari et al. 2019; Lakhchaura et al. 2019). In early type galaxies (ETGs), which are the focus of this paper, observations have established a steep and tight correlation

between the total halo X-ray luminosity (L_X) and X-ray temperature, T_X , which is hard to be explained using the self similarity argument alone (Boroson et al. 2011; Kim & Fabbiano 2013, 2015; Babyk et al. 2018). Further, it has been established that hot atmospheres of ETGs cannot be created through the action of stellar feedback alone (Goulding et al. 2016; Werner et al. 2019). These clues suggest that AGN feedback plays significant role in moulding the properties of hot atmospheres around ETGs.

In numerical simulations, the AGN feedback is implemented via two modes. The nomenclature for these modes is diverse in the literature. Throughout this work, we refer to them as “cold” and “hot” modes, following Yuan et al. (2018b). Cold mode, also referred to as the “quasar mode” or “radiative mode”, operates in AGNs which are powered by cold accretion flow when the accretion rate is above $\sim 2\%$ Eddington rate ($\dot{M}_{\text{Edd}} \equiv 10L_{\text{Edd}}/c^2$). The main outputs in this mode are radiation and wind (Morganti 2017; Yuan et al. 2018b).

The hot mode, also the kinetic or jet or radio or mechanical mode, operates in AGNs which are powered by hot accretion flow when the mass accretion rate is below $\sim 2\%\dot{M}_{\text{Edd}}$. The outputs of the AGN in this mode are radiation, wind, and jet (Yuan et al. 2018b). It has been suggested that wind launched in this mode may prevent the gaseous atmosphere from cooling and forming stars, thereby maintaining the quiescent state of the galaxy (Yao et al. 2021, also

[★] E-mail:aditi.vijayan@anu.edu.au

[†] E-mail: miaoli@zju.edu.cn

[‡] E-mail: fyuan@shao.ac.cn

Zhu et al 2022 (in prep) for details), or even inducing quenching of the galaxy (Weinberger et al. 2017). Observationally, this mode has been identified in clusters from the presence of a cavity in the X-ray emission which is filled with radio emission (Werner et al. 2019, see for a review).

Unfortunately, works focussed on simulating AGN feedback simulation are quite diverse in the sense that different works adopt different models and not all the above-mentioned AGN physics has been properly incorporated (Naab & Ostriker 2017). Some simulations successfully reproduce key observations such as the presence of buoyant cavities (Gaspari et al. 2012, 2014), M_{\bullet} - σ relation (Sijacki et al. (2007); Booth & Schaye (2011); Teyssier et al. (2011); Choi et al. (2015), etc). One aspect where tension persists between simulations and observation is the X-ray emission properties of systems hosting an AGN.

Diffuse soft X-ray emission ($\lesssim 2$ keV) originates from hot gas within and around a galaxy. Such a diffuse emission has been observed and studied around star-forming galaxies (Yamasaki et al. 2009; Anderson & Bregman 2011; Dai et al. 2012; Anderson et al. 2016; Bogdán et al. 2013a,b, 2017; Lopez et al. 2020) as well as more massive galaxies (Anderson et al. 2015; Kim & Fabbiano 2015). The emission is usually characterised by the total X-ray luminosity (L_X) and the temperature of the emitting gas, T_X , estimated by fitting the X-ray spectrum by emission models. Simulations of early-type galaxies (ETGs) (Gaspari et al. 2012, 2014) report a lower than expected L_X and a break in the L_X - T_X relation neither of which are corroborated by observations (Babyk et al. 2018). Choi et al. (2015) analysed separately the effects of the two feedback mechanisms and found that their quasar (thermal) mode of feedback overestimates L_X by nearly two orders of magnitude. Cosmological simulations such as Illustris-TNG (Truong et al. 2020b) and EAGLE (Schaye et al. 2015) also report brighter than observed X-ray emission as a result of their respective AGN feedback recipes (Davies et al. 2019).

Apart from global X-ray properties such as L_X , the X-ray emission spectrum carries a wealth of information about the temperature and the chemical abundance of the hot emitting gas. Usually, spectral fitting models, based on simplifying assumptions about the underlying emitting plasma, are used to derive the temperature from the spectrum (T_{spec}). Studies of simulated emission from clusters have found that the spectra-derived temperature T_{spec} may differ from emission-weighted temperature (T_{ew}), leading to underestimation in the latter of up to $\sim 20\%$ (Mazzotta et al. 2004; Rasia et al. 2005; Vikhlinin 2006). Spectrum-derived temperature estimates of diffuse gas around galaxies are also dependent on whether the fitting models use a single or multi-temperature components (Li & Wang 2013; Wu et al. 2020).

Previous X-ray studies of diffuse gas around isolated galaxies have been limited by the spectral resolution, sensitivity, and the magnitude of the field of view of the telescopes. Upcoming X-ray missions such Hot Universe Baryon Survey (HUBS) are specifically designed to study the hot, diffuse gas around galaxies, groups and cluster (Cui et al. 2020). With respect to AGN feedback occurring in ETGs, this presents an opportunity to study the observational effects of the hot and cold feedback mechanisms on the circumgalactic medium (CGM) around such galaxies. Further, a comparison with observations can indicate how well various AGN feedback recipes, implemented in different simulations, emulate the physical processes occurring in nature and whether some of the discrepancies with respect to observation can be removed.

In this project, we aim to understand the X-ray properties of the ISM within and the CGM around isolated elliptical galaxies. Specifically, we analyse the relationship between an estimate of X-ray

temperature, obtained from the emission spectrum, and the physical temperature of the gas in the galaxy. We analyse results from high-resolution simulations presented in Yuan et al. (2018b), which follow the evolution of an isolated elliptical galaxy (i.e., not considering galaxy merger and cosmological inflow to the galaxy) based on the *MACER* code. The two main features of the model are that: 1) the black hole accretion rate is precisely determined because the inner boundary of the simulation and is typically ten times smaller than the Bondi radius of the accretion flow and, 2) the state-of-the-art AGN physics is incorporated into the code, including the wind and radiation as a function of mass accretion rate. We briefly introduce the key components of the model in Section 2. In Section 3, we discuss the major results of our analysis and we present the major conclusions in Section 4.

2 MODELS

In this section we give a brief summary of the *MACER* simulations presented in Yuan et al. (2018b). Readers are also referred to Yuan et al. (2018a) for an overview of the *MACER* code. *MACER* are a set of 2D, axi-symmetric simulations which focus on the evolution of a single elliptical galaxy, with the inner and outer boundaries being ~ 2 pc and 500 kpc, respectively. A resolution as high as ~ 0.3 pc is achieved at the inner boundary. The Bondi radius of the accretion flow is typically ~ 15 pc (Yao et al. 2021), which is several times larger than the inner boundary of the simulation, thus the outer boundary of the accretion flow is well resolved. Once the accretion rate at the inner boundary of our simulation domain is calculated, we can safely combine the accretion physics as subgrid model and precisely calculate the mass accretion rate of the AGN at the black hole horizon. This is crucial to determine the strength of the AGN feedback.

According to the value of the mass accretion rate, the accretion is divided into “cold” and “hot” modes, bounded by $\sim 2\% L_{\text{Edd}}$ (Yuan & Narayan 2014). Radiation and wind are present in both modes while jet is perhaps present only in the hot mode¹. The properties of the wind in the cold mode, including the velocity and mass flux as a function of AGN luminosity, are taken from observations (Gofford et al. 2015). Wind in the hot mode has been intensively studied in recent years by magnetohydrodynamical numerical simulations (Yuan et al. 2012; Narayan et al. 2012; Yuan et al. 2015; Yang et al. 2021). In the observational side, we are accumulating more and more observational evidences for wind from hot accretion flows, including the supermassive black hole in our Galactic center (Wang et al. 2013; Ma et al. 2019), low-luminosity AGNs (Cheung et al. 2016; Park et al. 2019; Shi et al. 2021, 2022). Especially, Shi et al. (2021, 2022) have found the most direct evidences for winds in two prototype low-luminosity AGNs by detecting the blue-shifted emission lines. But still, we have not obtained good constrain to the hot wind properties, therefore we adopt the properties of wind from GRMHD simulations of Yuan et al. (2015).

Wind and radiation are injected at the inner boundary of the simulation domain as the boundary conditions. Their energy and momentum interaction with the gas in the host galaxy is calculated self-consistently in the code. In addition to AGN feedback, the code also

¹ Maybe jets are also present in some cases when the accretion is in the cold mode, hinted by the existence of radio-loud quasars. This is still an unsolved problem. Jet has not been included in the hot mode in Yuan et al. (2018b) and it is being added into the code in Guo et al. (2022, in preparation).

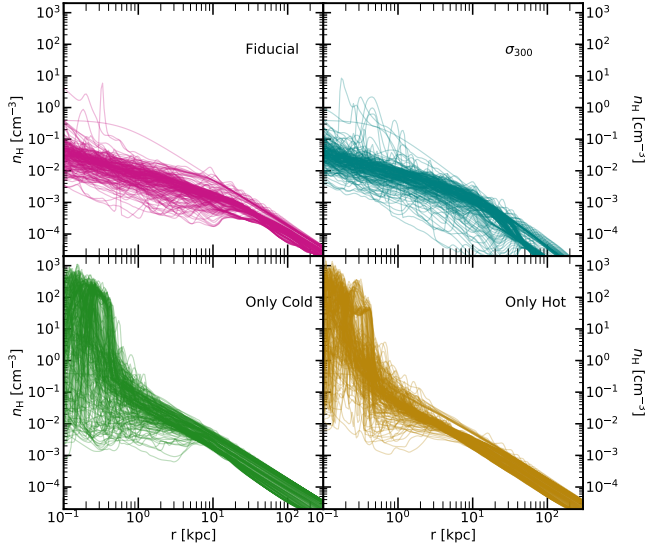


Figure 1. The radial variation of number density (n_{H}) for the four models. Each curve represents a different time in the simulation.

includes star formation and stellar feedback. We follow the evolution of the galaxy for ~ 2.5 Gyr up to the present redshift.

We consider four different models in the present work, as listed in Table 1, with different AGN feedback models and galaxy properties. The first “Fiducial” model is directly taken from Yuan et al. (2018b), in which the AGN feedback physics as mentioned above has been properly incorporated. Specifically, both “hot” and “cold” modes have been taken into account according to their accretion rates. In the “Only Cold” (“Only Hot”) model, irrespective of the accretion rate, we always adopt the physics of the cold (hot) mode for the descriptions of wind and radiation. In the “ σ_{300} ” model, the AGN physics is identical to the Fiducial model, but we change the the value of the velocity dispersion of the galaxy from 200 km s^{-1} to 300 km s^{-1} . Using these four models, we mimic the effects of different AGN feedback physics and galaxy size. One main caveat of these models is that we do not consider the effects of cosmological inflow. It is expected that it will affect the physical properties of the CGM of the galaxy. We will consider this effect in the future work.

3 RESULTS

3.1 Density and Temperature Distribution

We first discuss the temperature and density distributions of gas in different models. Figures 1 and 2 show the radial distribution of density and the emission-weighted temperature in the four models. Each curve in every panel represents one time in the simulation.

As expected, the density profiles are declining outward radially. Upto $r > 200$ kpc, the profiles are similar to those following the hydrostatic equilibrium. The profiles for “Only Hot” and “Only Cold” models are flat within 1 kpc and drop by five orders of magnitude beyond this radius. The “Fiducial” and “ σ_{300} ” have monotonically declining profiles up to $r \gtrsim 200$ kpc. We also note that the density profiles in the inner region ($r < 10$ kpc) of the “only hot” and “only cold” modes vary significantly in time, up to nearly four orders of magnitude. In the outer regions, $r > 10$ kpc, this feature is reversed, that is, in the “Only Hot” and “Only Cold” models there is hardly

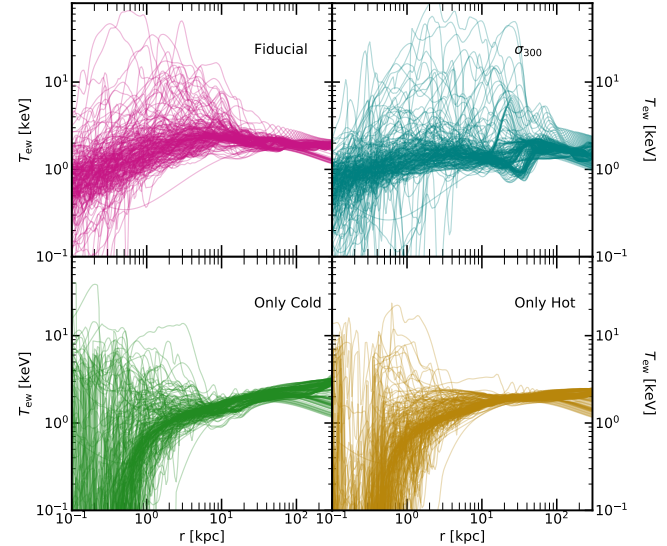


Figure 2. Identical to Figure 1, but instead of number density, we show the emission-weighted temperature, defined by Equation 1.

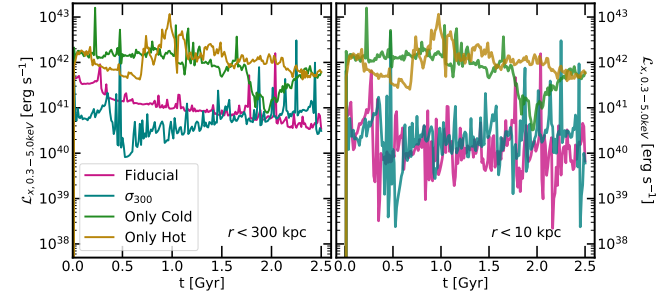


Figure 3. Temporal variation of the total soft (0.3–5.0 keV) X-ray luminosity for the four runs, calculated for $r < 300$ and $r < 10$ kpc.

any variation in density profiles, while for the “Fiducial” and “ σ_{300} ”, there is a greater variation.

We define the emission-weighted temperature as

$$T_{\text{ew}} = \frac{\int n^2 \Lambda(T) T dV}{\int n^2 \Lambda(T) dV}, \quad (1)$$

where $\Lambda(T)$ is the X-ray emissivity between 0.3–5.0 keV², T is the gas temperature and n is the gas number density. The radial profiles for four different models are shown in Figure 2. As for Figure 1, each curve represents a different time step in the evolution. Unlike the density profiles, the temperature profiles have a vary across the radial extent, from 0.1–3 keV.

The general trends of density and temperature of the “Fiducial” and “ σ_{300} ” models shown in the above two figures are not difficult to understand as they are similar to profile representing hydrostatic equilibrium. However, for “Only Cold” and “Only Hot” models, we can see that the density (temperature) rapidly increases (decreases) inward within ~ 1 kpc. As shown in Yuan et al. (2018b), the main energy input from the AGN is by wind. The significantly smaller

² This energy range is for estimating the emission-weighted temperature for *Chandra*-like low spectral resolution instrument.

Table 1. Model description

Name	Features
Fiducial	Identical to the one described in Yuan et al. (2018b) .
OnlyCold	Adopting the cold-mode AGN physics no matter what the value of the accretion rate.
OnlyHot	Adopting the hot-mode AGN physics no matter what the value of the accretion rate.
σ_{300}	The galaxy velocity dispersion is set to 300 km s ⁻¹ as compared to 200 km s ⁻¹ in the Fiducial run.

temperature (and thus larger density) in ‘‘Only Cold’’ and ‘‘Only Hot’’ models compared to the Fiducial model is because the energy input from wind is much weaker in the former two cases. For the ‘‘Only Cold’’ model, compared to the Fiducial model, the wind power remains same when the accretion is in the cold mode. But when the accretion rate is low and the accretion is in the hot mode, the wind described by the ‘‘cold-mode physics’’ will be weaker than that described by the ‘‘hot-mode physics’’. Similarly, for the ‘‘Only hot’’ model, the wind power remains same when the accretion rate is low. But when the accretion rate is high, the wind described by the ‘‘hot-mode physics’’ will be weaker than that described by the ‘‘cold-mode physics’’.

The density and temperature distribution of the gas determines the X-ray luminosity of the system. We show the soft X-ray luminosity integrated from the whole galaxy plotted against the simulation time in Figure 3. To obtain the luminosity from the simulation data, we use APEC emissivity tables between 0.3 and 5.0 keV. We show the luminosity from the entire simulation domain (left panel) as well as that from the ISM, $r < 10$ kpc. For all the models, the stochasticity in the density and temperature profiles is translated into the temporal variations in the luminosity.

Given the high stochasticity of the density and temperature profiles of the ‘‘Only Hot’’ and ‘‘Only Cold’’ models in the ISM, there is significant variation in the total luminosity from this region. Further, these models have higher luminosity because on an average they have higher density values, especially in the ISM of the galaxy.

3.2 Extracting Pure Emission Spectra

We use pyatomDB ([Foster & Heuer 2020](#)) to generate a spectral emission from a parcel of gas over a wide range of temperature, density and metallicity. pyatomDB ([Heuer et al. 2021](#)) is a database for modelling the X-ray emission from collisionally-ionised plasma. The users have the option to convolve the spectra generated with an instrument response to produce a realistic spectrum. In this Section, we discuss the spectrum derived temperature, $T_{\text{spec,low}}$ and high-spectral resolution instruments.

We use the density, temperature and metallicity information from each cell in the ISM region ($r < 10$ kpc) of the simulation domain as an input for pyatomDB and generate a spectrum for every cell. For low resolution T_{spec} , we set the instrument response in the pyatomDB session corresponding to the instrument AISCC (on the *Chandra* telescope having a resolution of ~ 130 eV) and for the high resolution T_{spec} , we use the response for HUBS telescope³. We then add the spectrum emitted by each cell and sum it up to produce a single spectrum for the entire simulation domain. Figure 4 shows the high-resolution spectra for the four models, after 1.25 Gyr of evolution,

³ HUBS is an upcoming X-ray telescope designed specifically to observe hot gas around galaxies, having a $1^\circ \times 1^\circ$ FoV and a spectral resolution of 2 eV ([Cui et al. 2020](#)). The energy range of HUBS is 0.5 – 2.0 keV, therefore, we show the spectra in this energy range.

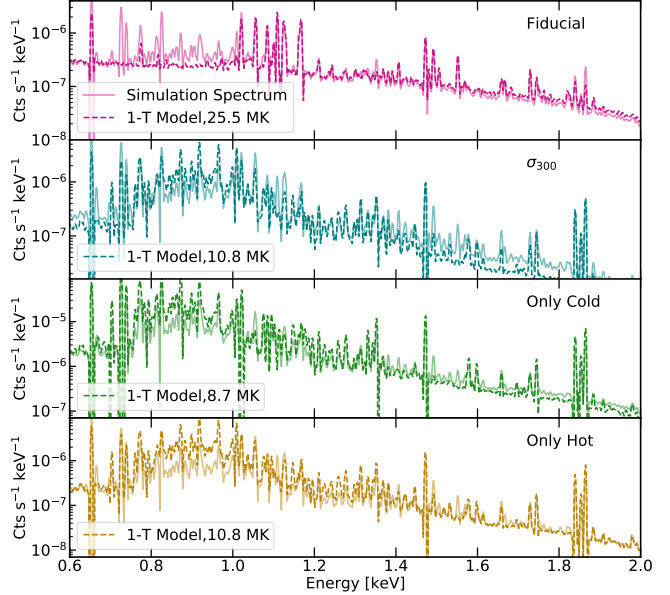


Figure 4. The simulation spectra after 1.25 Gyr of evolution, which roughly marks the midway of the simulation for the different AGN models, and their comparison with the spectra produced by the 1-T model. The solid lines represent the simulation spectra, generated using pyAtomDB, as described in the text. The best-fit spectra are shown by the dashed curve. The spectra are generated using the gas between 0.1 – 10.0 kpc, that is the ISM of the galaxy. The number indicates the fitting temperature, T_{spec} .

in dashed lines. As expected, the emission decreases with increasing energy.

We extract the temperature of the X-ray emitting gas from the spectra, which is an observable quantity obtained by fitting models to the observed spectrum. We use the recipe followed by observers to extract a spectral temperature, T_{spec} . We fit the spectra using a 1-T fitting model similar to the fitting methods described in ([Truong et al. 2020b](#)), but with some minor modifications described below. The 1-T model assumes that the observed spectrum is the result of emission from gas at a single temperature. Using temperature as a free parameter, we fit the simulation spectrum for every time step of the simulation. We then compare the simulation spectrum with a set of ideal spectra generated using pyAtomDB. To estimate the best-fit temperature, we minimized a statistical quantity, called the Wasserstein distance ([Rubner et al. 1998](#)), between the simulation spectrum and the ideal spectrum generated at that temperature. The temperature corresponding to the minimum distance is taken to be the best-fit temperature, which we denote as T_{spec} .

In Figure 4, we show the simulation spectrum from the ISM as well as the corresponding spectrum from the best-fit single temperature model after ~ 1.25 Gyr of evolution. The solid curves in each panel represent the spectrum from the simulations, while the dashed curves are the best-fit spectra, obtained using the procedure outlined above,

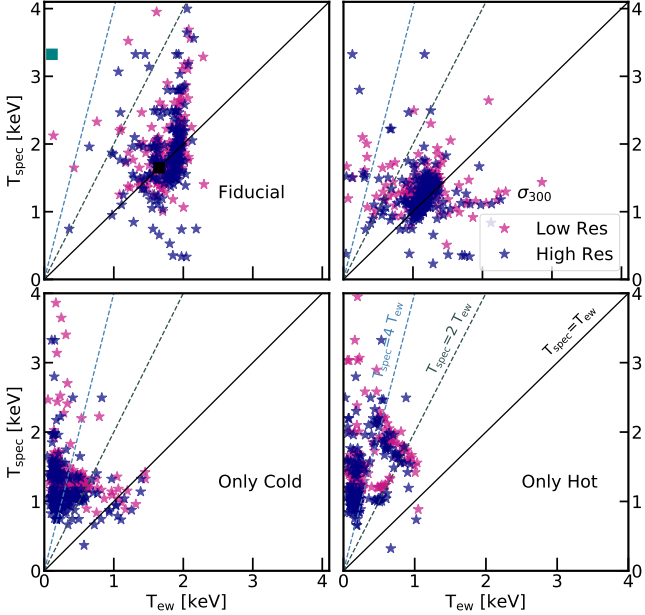


Figure 5. The distribution of T_{spec} with the emission-weighted temperature, T_{ew} , indicating the discrepancy between the two quantities for various models. Each star corresponds to a different time step in the simulation. We show T_{spec} generated for low (~ 130 eV) and high (~ 2 eV) spectral resolution instruments. For reference, we show curve corresponding to $T_{\text{spec}} = T_{\text{ew}}$ (black, solid), $= 2T_{\text{ew}}$ (grey, dashed) and $= 4T_{\text{ew}}$ (blue, dashed). We have used the region between $0.1 - 10$ kpc for estimating the two temperatures. The black and teal points indicate time steps for which $T_{\text{spec}} >$ and $T_{\text{spec}} \sim T_{\text{ew}}$, respectively. We show the luminosity-weighted temperature-density histogram for these time steps in Figure 7. Though there are time steps in all the models, for which T_{spec} accurately predicts T_{ew} , it is not always the case.

with the fitting temperature in the bottom left corner. The spectra obtained from 1-T model provides a reasonable fit for the simulation data, even though it is quite simplistic. However, it is not a perfect fit as it misses out, for e.g., low temperature emission (< 1.0 keV) in Fiducial model and relatively high energy emission (> 1.6 keV) in the σ_{300} model. We note that the spectra corresponding to σ_{300} , “Only Cold” and “Only Hot” models show similar hump-like feature around $0.8 - 1.0$ keV, while the Fiducial run does not. Note that the fitting temperatures are different for all the four models.

3.3 Comparing Spectral Temperature with Emission-Weighted Temperature

The physical interpretation of T_{spec} is that it represents the emission-weighted temperature of the gas. To assess how accurate this interpretation is, we compare the T_{spec} with the emission-weighted temperature, T_{ew} , calculated using Equation 1. From the simulation data, we know the emission-weighted temperature exactly. For each time step, we now have a pair of temperatures- T_{ew} and T_{spec} . Though both temperatures are obtained from the simulation data, T_{spec} is the temperature that derived from spectra, while T_{ew} is the *actual* temperature of the gas. Such a comparison, between these two different temperatures, is not possible with observations.

Figures 5 and 6 show scatter plots between T_{ew} and T_{spec} for the ISM and the CGM ($r > 10$ kpc), respectively. The spectrum from the ISM (CGM) is obtained by including only those cells that

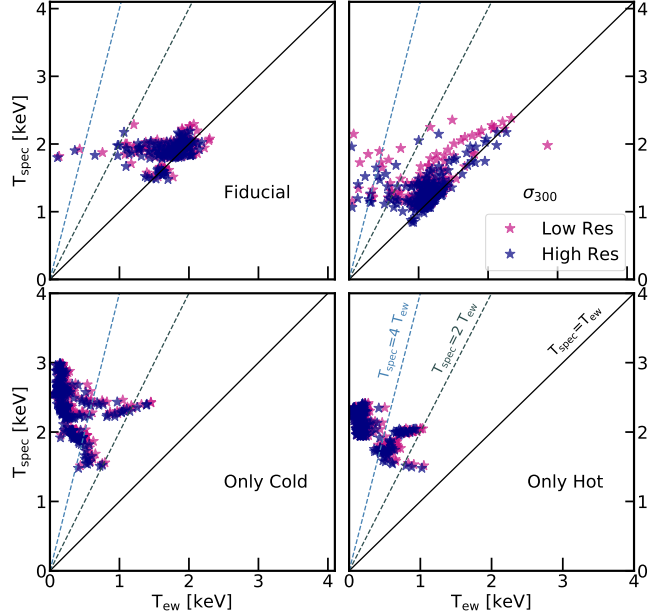


Figure 6. Identical to Figure 5, but for the region between $10 - 300$ kpc.

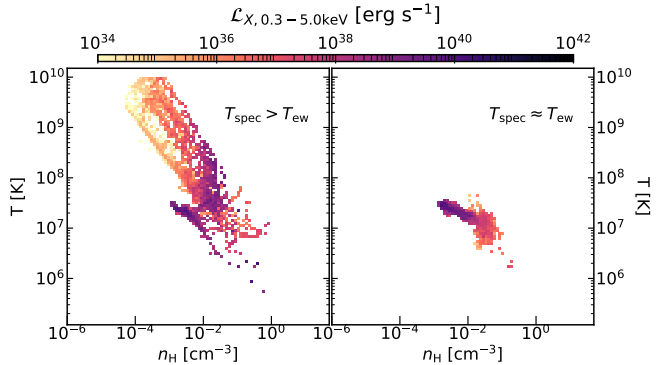


Figure 7. The temperature-density distribution of luminosity for two time steps of the Fiducial run. The left and right panel correspond to the teal and black squares in Figure 5, respectively.

lie within (without) 10 kpc.⁴ We obtain T_{spec} from the spectra for high-resolution (magenta points) and low-resolution (navy points) instruments, for several time steps. If the two temperatures are identical, they should fall on the solid black line which represents the equality $T_{\text{spec}} = T_{\text{ew}}$. In the figures, we also show lines corresponding to $2T_{\text{ew}}$ and $4T_{\text{ew}}$. While there exist some time steps when the predicted T_{spec} is equal or close to the physical T_{ew} , the equality does not hold true for most time steps during the simulation. Overall, we note that for both inner- and outer-CGM, the predicted T_{spec} overestimates T_{ew} by a factor of $\gtrsim 4$.

There are considerable differences in the $T_{\text{spec}} - T_{\text{ew}}$ distribution between the ISM and CGM. For the CGM, the predicted T_{spec} by

⁴ Actual spectra from the ISM region will possess contribution from the intervening gas between the observer and the CGM. However, from the radial surface brightness plot (Figure 12) we estimate that this contribution will be negligible and therefore, we ignore it for our analysis.

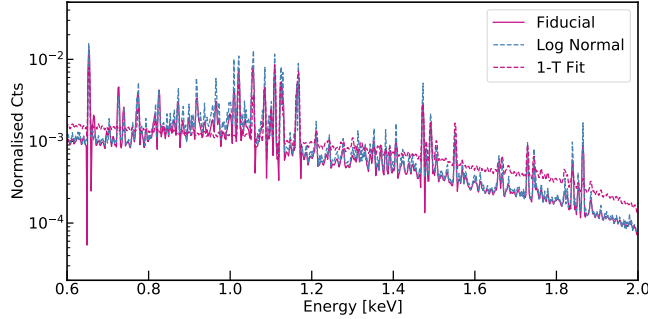


Figure 8. Comparison of the spectrum from the log normal model of temperature distribution, the Fiducial model at the same time step and the fit corresponding to the single temperature fit.

the lower resolution instrument are close to their higher resolution counterpart, as the navy and magenta points are overlapping for several time steps, while for ISM the two predict different T_{spec} .

To understand the source of the discrepancy between T_{spec} and T_{ew} , we show the luminosity-weighted temperature-density histogram of two time steps in Figure 7. We have chosen these particular time steps from Figure 5 where these are shown in black and teal squares in the panel for the Fiducial run. The teal square corresponds to a time step for which $T_{\text{spec}} > T_{\text{ew}}$ at 0.275 Gyr and for the black square at 1.64 Gyr the two temperatures are nearly identical. For Figure 7, we distribute the gas in 0.1 – 10 kpc in several temperature and density bins and weighted using the soft X-ray luminosity. The gas distribution corresponding to the time step for which $T_{\text{spec}} > T_{\text{ew}}$ (teal point in Figure 5) has a wide temperature range ($10^3 \text{ K} < T < 10^{10} \text{ K}$). The luminosity is dominated by gas at 10^{7-10} K , therefore its spectral temperature is $\sim 2 \times 10^7 \text{ K}$ ($\equiv 2.0 \text{ keV}$). However, the galaxy hosts significant amount of mass at much lower temperatures. While this lower temperature gas ($T < 10^6 \text{ K}$) does not contribute significantly to the total luminosity, it contributes towards lowering T_{ew} . As a result, T_{spec} is greater than T_{ew} .

The right panel of Figure 7 corresponds to a time step for which T_{spec} predicts T_{ew} correctly (both equal to $\sim 1.9 \text{ keV}$). At this time step, the luminosity distribution in the temperature-density plane is relatively narrow and though there is mass at higher temperatures ($> 10^6 \text{ K}$), it does not dominate the emission. As a result, both the temperatures are close to each other. The reason why there is copious amount of extremely hot at 0.275 Gyr is because it corresponds to a local peak in the luminosity (perhaps corresponding to a peak in the luminosity). We conclude here that T_{spec} , estimated using the single temperature spectral fitting model, reliably predicts T_{ew} only when the gas in the galaxy possesses a narrow temperature distribution.

3.4 Fitting Log Normal Model to Spectra

In the previous Section, we show that the discrepancy between T_{spec} and T_{ew} are considerable if the actual temperature distribution of the underlying gas is over several orders of magnitude. In such a case, fitting the spectrum with a single temperature emission model is not entirely physical. It has been suggested that a log-normal temperature distribution is better suited to represent gas that occupies a wide range in temperature (Vijayan & Li 2022). To assess this, we re-fit the spectrum at the time step, represented by the teal square in Figure 5, at which there is large discrepancy between T_{spec} and T_{ew} .

As indicated in the left panel of Figure 7, the X-ray emitting gas lies between $\sim 10^{7-10} \text{ K}$. To obtain a spectrum from a log-normal

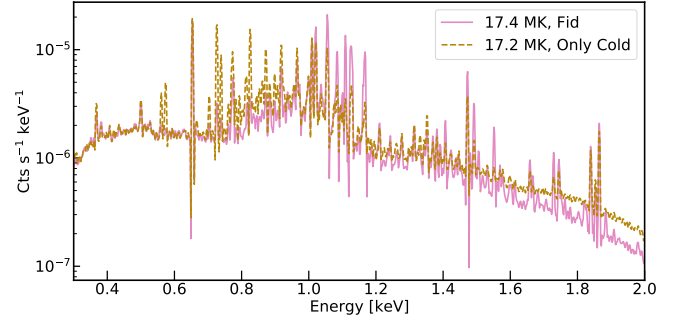


Figure 9. The spectra from the Fiducial and “Only Cold” simulations between 0.1 and 10 kpc. The spectra have been normalised with respective total luminosity.

distribution, we construct a box having dimensions identical to the simulation domain. The values of the density and metallicity fields are same as that of the simulation box. For every cell in the box, we extract a temperature value from a log-normal number distribution with a peak temperature at $\sim 2 \times 10^7 \text{ K}$ and a width of 0.4 dex in temperature. We choose the peak temperature from mass-weighted temperature distribution of the gas and the width of the log-normal is identical to that used in the analysis of (Vijayan & Li 2022). We follow the procedure described in Section 3.2 to extract the spectrum from the log-normal temperature distribution.

In Figure 8, we show the spectrum from the simulation (solid curve), the single temperature fit as well as the from the log-normal temperature distribution (dashed curves). We note here that for this particular time step, the T_{spec} from single temperature fit is $\sim 3 \text{ keV}$, while $T_{\text{ew}} \sim 0.3 \text{ keV}$. As can be seen from Figure 8, the single temperature fit is unable to reproduce the simulation spectrum at both high and low energies. However, the spectrum generated from the log-normal distribution is able to reproduce the spectrum well across the entire energy range because it is able to capture the wide temperature distribution of the gas.

3.5 Mock HUBS Spectrum

In Figure 9, we show the high-resolution spectrum for the Fiducial and “Only Cold” models at the same time step and fit by nearly identical single temperature fits ($T_{\text{spec}} \sim 17 \text{ MK}$). Despite identical fitting temperature, the spectra are not identical. The differences are especially stark in the 0.7 – 1.0 and $\gtrsim 1.6 \text{ keV}$ range. The feature in the 0.7 – 1.0 keV range are associated with Fe-line complexes which are very sensitive to the gas temperature (Böhringer & Werner 2010). To explore whether such features in the spectrum can be used as a diagnostic for discriminating between AGN models and galaxy sizes, we estimate the fractional 0.7 – 1.2 keV line width which is the ratio between the counts in 0.7 – 1.2 keV to the counts in the full energy range (0.3 – 2.0 keV) for all the models. To understand how this quantity changes with radius, in Figure 10 we show it as a function of radius. The binning in radius is narrower (10 kpc wide) for $r < 60 \text{ kpc}$ and wider (100 kpc) for radii larger than 60 kpc. This is because that temperature and density profiles are have lesser variation for larger radii (Figures 2 and 1). The line-width ratios have been averaged over all the timesteps.

The fractional line-width for σ_{300} shows a trend vastly different from the other three models. Unlike the other three models, at radii close to the centre, the fractional line-width is relatively small. It peaks at around $\sim 20 \text{ kpc}$, falls off upto 60 kpc and increase thereafter.

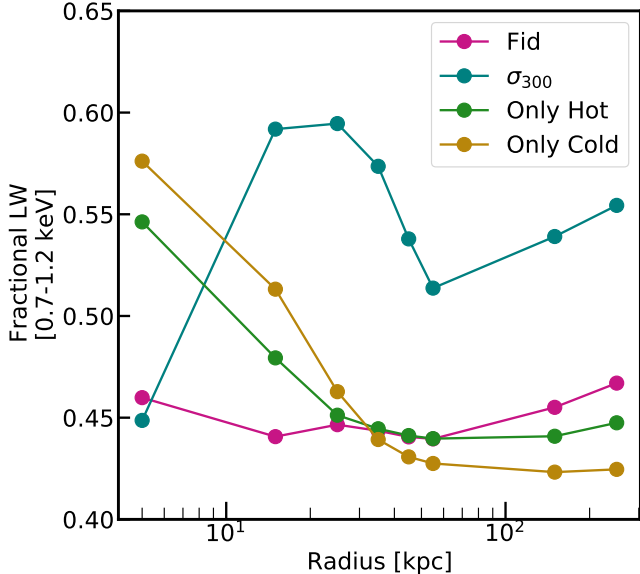


Figure 10. The ratio of the counts between 0.7 – 1.2 keV and the total counts for 0.2 – 2.0 keV for different runs.

The “Only Hot” and “Only Cold” models show trends similar to each other. The fractional line-width is strongest close to the centre, which has the highest density and temperature values and it flattens out at larger radii. The Fiducial fractional line-width remains nearly flat for the entire radial domain. From this Figure, we can conclude that fractional line-width should be able to distinguish

3.6 Simulating HUBS Emission

We convert the 2D spherical data from the simulations into 3D Cartesian data using the assumption of axi-symmetry. We do this conversion in order to use the python package, pyXSIM, for modelling X-ray emission from the simulation data set. Because this 2D to 3D is a computationally expensive process, we use a much lower resolution for the Cartesian data.

Using a distance of 15 Mpc and an exposure time of 300 ks, we generate a mock HUBS image of the galaxy, using the Fiducial model. We excise the innermost 600 pc of the galaxy as it is excessively bright, and produce X-ray emission from the gas within 300 kpc of the galaxy. We provide arbitrary RA and Dec values and turn off contribution from various backgrounds and foregrounds. We select a time step (1.25 Gyr, which is half way through the simulation) and generate a mock image based on the underlying density and temperature distribution at this time step. The resulting image generated from such a synthetic observation is shown in Figure 11. As expected, the region close to the centre of the galaxy is the brightest and the brightness decreases radially outwards. This is expected since most of the volume of the outer-CGM is filled with low density gas (top-right panels of Figures 1 and 2). We therefore expect the X-ray brightness to fall off sharply away from the centre. At the scale shown in Figure 11, the distinguishing features in the gas density and temperature profiles are smoothed out.

We repeat the process and produce mock images for all the models discussed in this paper. For each of these runs, we radially average the surface brightness profile and obtain a radial intensity plot. We divide the pixels of the mock image into equal radially spaced 100 annular regions and sum up the total number of photon counts in each

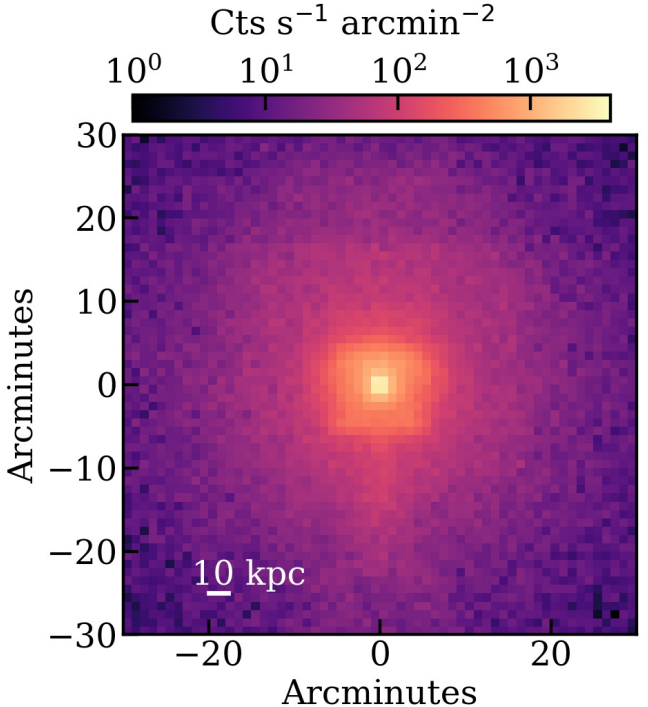


Figure 11. Mock image of the Fiducial run using HUBS. This is a 300 ks observation. The galaxy is at a distance of 15 Mpc.

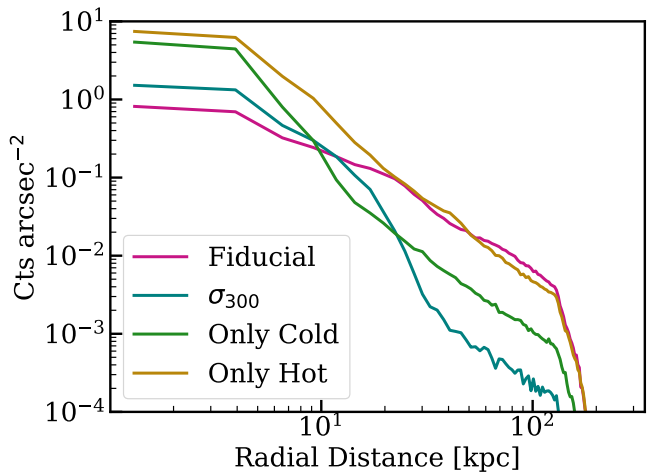


Figure 12. Surface brightness profile of the mock image for the various runs, corresponding to the time step half-way through the simulation at ~ 1 Gyr.

region. We divide the total photon count by the area of the annular region to normalise and plot it against the physical distance along the radius of the galaxy. We show the annulus-averaged brightness in Figure 12. Though T_{spec} values for “Only Cold” and “Only Hot” models are similar, 18 and 14 MK, respectively, their radial profiles have different slopes, indicating that radial surface brightness profiles might hold clue to the mode of accretion taking place in the galaxy’s AGN.

4 DISCUSSION & CONCLUSIONS

4.1 Comparison with Other Works

We have undertaken a systematic study of the relationship between two estimates of gas temperatures, viz, T_{spec} and T_{ew} . While T_{spec} is obtained from spectral analysis of X-ray emission from hot gas in the ISM and the CGM around elliptical galaxies, T_{ew} is estimated from the simulation data. The properties of the hot gas are intrinsically related to the properties of the SMBH hosted by the galaxy and the correlations between the two have been studied via observations (Lakhchaura et al. 2018; Gaspari et al. 2019; Lakhchaura et al. 2019) and simulations (Gaspari et al. 2014; Truong et al. 2020b,a). While these works focus on quantities such as the black hole mass, the total X-ray luminosity etc, our work aims to understand the spectral properties of the emission. Such a study is critical in the context of the upcoming X-ray telescope, HUBS, which has a large FoV ($1^{\circ} \times 1^{\circ}$) and \sim eV spectral resolution (compared to ~ 100 eV of *Chandra*).

The high resolution of the X-ray spectrum will provide us with abundant information about the temperature distribution of the hot gas. In this respect, it is critical to evaluate the relationships between the extracted spectral temperature and the actual gas temperature. Mazzotta et al. (2004) address the discrepancy between the *Chandra* spectral temperatures of galaxy clusters and their physical equivalents from simulations. They find that the spectroscopic temperature obtained from X-ray observations is always lower than the emission-weighted temperature in the cluster. In our analysis, we find that T_{spec} may be higher than T_{ew} by a factor of ~ 4 (Figures 5 and 6).

4.2 Conclusions

We have analysed 2D axi-symmetric simulations of the evolution of an elliptical galaxy under the influence of feedback from the SMBH at its centre. We are interested in the X-ray emission from the hot ($T > 10^6$ K) diffuse gas in the ISM and the CGM of such a galaxy. We explore four sets of simulations representing the different forms of feedback (“Fiducial”, “Only Hot”, and “Only Cold”) and different galaxy size (“ σ_{300} ”). We follow the galaxy evolution for a period of ~ 2 Gyr, over which the SMBH undergoes several outburst phases resulting in radially declining density and temperature profiles (Figures 1 and 2). Because of the stochasticity of the outbursts, the soft X-ray luminosity (0.3 – 5.0 keV) varies considerably over the simulation time period (Figure 3). We use pyAtomDB for estimating the spectral temperature of the gas in the simulation for low and high spectral resolutions and compare it with the emission weighted temperature.

Our main conclusions are as follows-

- (i) The spectral temperature, estimated using spectral analysis, is different from the emission-weighted temperature by a factor of few.
- (ii) The low- (resolution ~ 130 eV) and high-resolution (resolution ~ 2 eV) instruments produce nearly the same predictions for the T_{spec} .
- (iii) The difference between T_{spec} and T_{ew} arise because the spectral fitting model (a single temperature fit) is not able to capture the gas distribution accurately. Using a more physically motivated model, such as the log-normal model, can potentially alleviate the discrepancies between the two temperatures (Figure 8).
- (iv) Even if T_{spec} is similar for different models, the underlying gas properties might be different. Such differences appear only upon analysis of the full spectra (Figure 9).
- (v) The ratio of counts between 0.7 – 1.2 keV, a range corre-

sponding to Fe-line emission, can potentially be a diagnostic tool for discriminating between different accretion models (Figure 10).

(vi) The surface brightness maps could also hold clues about the exact mode of accretion taking place within the galaxy, as the radial profiles of surface brightness possess different slopes for the various runs (Figure 12).

ACKNOWLEDGEMENTS

We thank Drs. Wei Cui and Jiangtao Li for helpful discussions and comments. AV, BZ, and FY are supported in part by the Natural Science Foundation of China (grants 12133008, 12192220, and 12192223), and the China Manned Space Project (No. CMS-CSST-2021-B02). LCH was supported by the National Science Foundation of China (11721303, 11991052, 12011540375) and the China Manned Space Project (CMS-CSST-2021-A04, CMS-CSST-2021-A06). The analysis, presented in this paper, was done using the High Performance Computing Resource in the Core Facility for Advanced Research Computing at Shanghai Astronomical Observatory. AV would like to thank the staff maintaining the facility for their support.

DATA AVAILABILITY

The data underlying this paper will be shared on reasonable request to the corresponding author.

REFERENCES

Anderson M. E., Bregman J. N., 2011, *ApJ*, **737**, 22
 Anderson M. E., Gaspari M., White S. D. M., Wang W., Dai X., 2015, *MNRAS*, **449**, 3806
 Anderson M. E., Churazov E., Bregman J. N., 2016, *MNRAS*, **455**, 227
 Babyk I. V., McNamara B. R., Nulsen P. E. J., Hogan M. T., Vantyghem A. N., Russell H. R., Pulido F. A., Edge A. C., 2018, *ApJ*, **857**, 32
 Bogdán Á., Forman W. R., Kraft R. P., Jones C., 2013a, *ApJ*, **772**, 98
 Bogdán Á., Forman W. R., Kraft R. P., Jones C., 2013b, *ApJ*, **772**, 98
 Bogdán Á., Bourdin H., Forman W. R., Kraft R. P., Vogelsberger M., Hernquist L., Springel V., 2017, *ApJ*, **850**, 98
 Bogdán Á., Lovisari L., Volonteri M., Dubois Y., 2018, *ApJ*, **852**, 131
 Böhringer H., Werner N., 2010, *A&ARv*, **18**, 127
 Booth C. M., Schaye J., 2011, *MNRAS*, **413**, 1158
 Borošon B., Kim D.-W., Fabbiano G., 2011, *ApJ*, **729**, 12
 Cheung E., et al., 2016, *Nature*, **533**, 504
 Choi E., Ostriker J. P., Naab T., Oser L., Moster B. P., 2015, *MNRAS*, **449**, 4105
 Cui W., et al., 2020, *Journal of Low Temperature Physics*, **199**, 502
 Dai X., Anderson M. E., Bregman J. N., Miller J. M., 2012, *ApJ*, **755**, 107
 Davies J. J., Crain R. A., McCarthy I. G., Oppenheimer B. D., Schaye J., Schaller M., McAlpine S., 2019, *MNRAS*, **485**, 3783
 Fabian A. C., 2012, *ARA&A*, **50**, 455
 Foster A. R., Heuer K., 2020, *Atoms*, **8**, 49
 Gaspari M., Brighenti F., Temi P., 2012, *MNRAS*, **424**, 190
 Gaspari M., Brighenti F., Temi P., Ettori S., 2014, *ApJ*, **783**, L10
 Gaspari M., et al., 2019, *ApJ*, **884**, 169
 Gofford J., Reeves J. N., McLaughlin D. E., Braito V., Turner T. J., Tombesi F., Cappi M., 2015, *MNRAS*, **451**, 4169
 Goulding A. D., et al., 2016, *ApJ*, **826**, 167
 Heuer K., Foster A. R., Smith R., 2021, *ApJ*, **908**, 3
 Kim D.-W., Fabbiano G., 2013, *ApJ*, **776**, 116
 Kim D.-W., Fabbiano G., 2015, *ApJ*, **812**, 127
 Lakhchaura K., et al., 2018, *MNRAS*, **481**, 4472
 Lakhchaura K., Truong N., Werner N., 2019, *MNRAS*, **488**, L134
 Li J.-T., Wang Q. D., 2013, *MNRAS*, **428**, 2085

Lopez L. A., Mathur S., Nguyen D. D., Thompson T. A., Olivier G. M., 2020, *ApJ*, **904**, 152

Ma R.-Y., Roberts S. R., Li Y.-P., Wang Q. D., 2019, *MNRAS*, **483**, 5614

Mazzotta P., Rasia E., Moscardini L., Tormen G., 2004, *MNRAS*, **354**, 10

Morganti R., 2017, *Frontiers in Astronomy and Space Sciences*, **4**, 42

Naab T., Ostriker J. P., 2017, *ARA&A*, **55**, 59

Narayan R., Sadowski A., Penna R. F., Kulkarni A. K., 2012, *MNRAS*, **426**, 3241

Park J., Hada K., Kino M., Nakamura M., Ro H., Trippe S., 2019, *ApJ*, **871**, 257

Rasia E., Mazzotta P., Borgani S., Moscardini L., Dolag K., Tormen G., Diaferio A., Murante G., 2005, *ApJ*, **618**, L1

Rubner Y., Tomasi C., Guibas L., 1998, in Sixth International Conference on Computer Vision (IEEE Cat. No.98CH36271). pp 59–66, doi:10.1109/ICCV.1998.710701

Schaye J., et al., 2015, *MNRAS*, **446**, 521

Shi F., Li Z., Yuan F., Zhu B., 2021, *Nature Astronomy*, **5**, 928

Shi F., Zhu B., Li Z., Yuan F., 2022, *ApJ*, **926**, 209

Sijacki D., Springel V., Di Matteo T., Hernquist L., 2007, *MNRAS*, **380**, 877

Teyssier R., Moore B., Martizzi D., Dubois Y., Mayer L., 2011, *MNRAS*, **414**, 195

Truong N., Pillepich A., Werner N., 2020a, arXiv e-prints, p. arXiv:2009.06634

Truong N., et al., 2020b, *MNRAS*, **494**, 549

Vijayan A., Li M., 2022, *MNRAS*, **510**, 568

Vikhlinin A., 2006, *ApJ*, **640**, 710

Wang Q. D., et al., 2013, *Science*, **341**, 981

Weinberger R., et al., 2017, *MNRAS*, **465**, 3291

Werner N., McNamara B. R., Churazov E., Scannapieco E., 2019, *Space Sci. Rev.*, **215**, 5

Wu X., Mo H., Li C., Lim S., 2020, *ApJ*, **903**, 26

Yamasaki N. Y., Sato K., Mitsuishi I., Ohashi T., 2009, *PASJ*, **61**, S291

Yang H., Yuan F., Yuan Y.-F., White C. J., 2021, *ApJ*, **914**, 131

Yao Z., Yuan F., Ostriker J. P., 2021, *MNRAS*, **501**, 398

Yuan F., Narayan R., 2014, *ARA&A*, **52**, 529

Yuan F., Bu D., Wu M., 2012, *ApJ*, **761**, 130

Yuan F., Gan Z., Narayan R., Sadowski A., Bu D., Bai X.-N., 2015, *ApJ*, **804**, 101

Yuan F., Ostriker J. P., Yoon D., Li Y.-P., Ciotti L., Gan Z.-M., Ho L. C., Guo F., 2018a, arXiv e-prints, p. arXiv:1807.05488

Yuan F., Yoon D., Li Y.-P., Gan Z.-M., Ho L. C., Guo F., 2018b, *ApJ*, **857**, 121

APPENDIX A: METALLICITY DISTRIBUTION

Apart from the density and temperature of the gas, its metallicity also affects the emission spectrum. In Figure A1, we show the radially averaged metallicity profiles for the four models. As in Figures 2 and 1, each curve represents a different time step and the black dashed curve is the temporal average. Similar to the density and temperature profiles, there is significant variation in the region close to the centre, while at larger radius the metallicity drops by nearly two orders and does not vary much with time.

APPENDIX B: COMPARING 2D AND 3D DATA

We have relied on generating 3D data from the axi-symmetric 2D simulations for the purpose of producing mock images and the radial surface brightness profiles in Section 3.6. In this Section, we compare the 3D and the original 2D data sets for the Fiducial run.

In the 2D simulations, the resolution is very high close to the centre (~ 0.5 pc) and decreases to (~ 10 kpc) at larger radius. As we are interested in the diffuse emission from CGM, for the 3D data conversion, we use a uniform grid size of 750 pc across the domain.

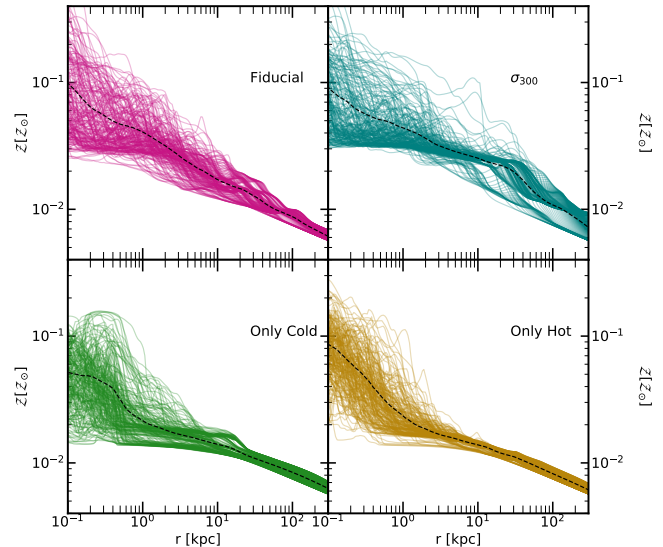


Figure A1. Radial dependence of the metallicity.

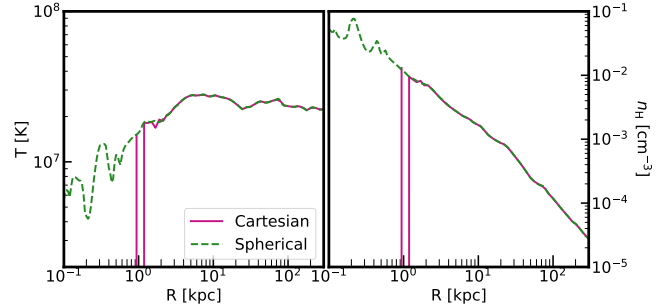


Figure B1. Comparison of the density and temperature profiles from the cartesian and spherical data.

In the inner regions of the 2D data, where the resolution is lesser than 750 pc, we average the quantities over multiple cells in the 2D data set for the corresponding spatial coordinates in the 3D data set. For the rest of cells in the 2D data set, we choose the value of the quantity in the nearest neighbour to the corresponding spatial location in the 3D.

To understand if the conversion between 2D and 3D data was faithful, we compare radially averaged temperature (left) and density (right) profiles for a particular timestep for the Fiducial run. The dip in the profiles, at around ~ 1 kpc, indicate the location of the first cell from the centre for the 3D data set. Beyond this radius, the profiles from 2D spherical data and 3D cartesian data are identical.

This paper has been typeset from a *TeX/LaTeX* file prepared by the author.